Effectuating tunable valley selection via multiterminal monolayer graphene devices

Shrushti Tapar◉ and Bhaskaran Muralidharan◉[*]

Department of Electrical Engineering, Indian Institute of Technology Bombay, Powai, Mumbai-400076, India

Valleytronics using two-dimensional materials opens unprecedented opportunities for information processing using a valley polarizer as a basic building block. Various methodologies, such as strain engineering, the inclusion of line defects, and the application of static magnetic fields, have been widely explored for creating valley polarization. However, these methods suffer from low transmission or lack of polarization directionality. To overcome the above limitations, we propose an all-electrical valley polarizer using zigzag edge graphene nanoribbons in a multiterminal device geometry. The proposed device can be gate-tuned to operate along two independent regimes: (i) a terminal-specific valley filter that utilizes band-structure engineering, and (ii) a parity-specific valley filter that exploits the parity selection rule in zigzag edge graphene. We show that the device exhibits intriguing physics in the multimode regime of operation affecting the valley polarization; we investigate various factors influencing polarization in wide-device geometries, such as optical analogs of graphene Dirac fermions, angle-selective transmission via *p-n* junctions, and the localization of edge states. Furthermore, we evaluate the performance of the proposed device structures in the presence of Anderson short-range disorder at the edges and the bulk, and we find it to be resilient to edge disorder even for a higher disorder strength. The device geometry is optimized to achieve maximum valley polarization, thereby paving the way for a physics-based tunable valleytronic device.

I. INTRODUCTION

The field of valleytronics provides the ability to control and manipulate the valley degree of freedom, opening new possibilities for energy-efficient devices for both classical and quantum information processing [1,2]. Two-dimensional (2D) materials such as graphene [3,4] and transition-metal dichalcogenides (TMDs) having momentum-separated nonequivalent valleys [5] are at the forefront of current research for valleytronic applications. Several techniques, such as introducing circularly polarized light [6–10], external magnetic fields [11,12], Rashba spin-orbit coupling (SOC), or exchange field [13–15], defect engineering [16–18], and strain engineering [19–23], are being typically employed to access the valleys [24]. However, in light of the current technological compatibility, an all-electrical control of the valley degree of freedom is typically desired. In 2D materials, valleys are electrically accessible via the presence of uneven Berry curvatures in the vicinity of the K and K' points [14,25–27]. While broken inversion symmetry in TMDs naturally induces a finite band gap and a valley-contrasting Berry curvature across the valleys [28], it is monolayer graphene that is a highly pursued and mature system for electronics applications [29,30]. Therefore, it is certainly worth delving into the physics of harnessing the valley degree of freedom in monolayer graphene.

The presence of inversion symmetry in monolayer graphene, however, complicates its potential for valleytronic applications. Given that the building block for valleytronics is the valley polarizer, several methods have been proposed for creating a high degree of polarization using monolayer graphene. These includes sublattice staggered potentials [31,32] that break the inversion symmetry [33,34], line-defect engineering [17,18], the application of uniform strain [20,21] and magnetic fields, and [35–38] the inclusion of various strain profiles [22,39–44], to name a few. Utilizing electrostatic potential barriers [45,46] that exploit the anisotropy of the Fermi surfaces for valley splitting caused by trigonal warping [47,48] is also a crucial aspect. While the aforementioned approaches exhibit polarization, they are limited by directionality and low transmission and are hard to realize on-chip.

The aim of this paper is hence to propose an all-electrical valley polarizer based on monolayer graphene nanoribbons (GNRs) that can be further gate-tuned to operate in two regimes; Regime 1: terminal-specific valley filter (TSVF) attributed to band-structure engineering, and Regime 2: parity-specific valley filter (PSVF) which uses the parity selection rule to operate as a valley filter. To put these ideas on a realizable footing, we propose a multiterminal *p-n* junction (PNJ) device structure and delve into the physics of complexities such as modal discrepancies at multiple terminals, related Dirac fermion optics, angle-selective transmission, and edge-state localization on the valley-filter operation.

The proposed multiterminal device [49,50], schematized in Fig. 1(a), exhibits the two independent operating regimes of valley polarization. In Regime 1, each terminal is designed to allow a specific valley component to transmit, depending on the edge-state slope polarity, enabling each terminal to act as a valley-selective transmitter. The PSVF regime, on the other
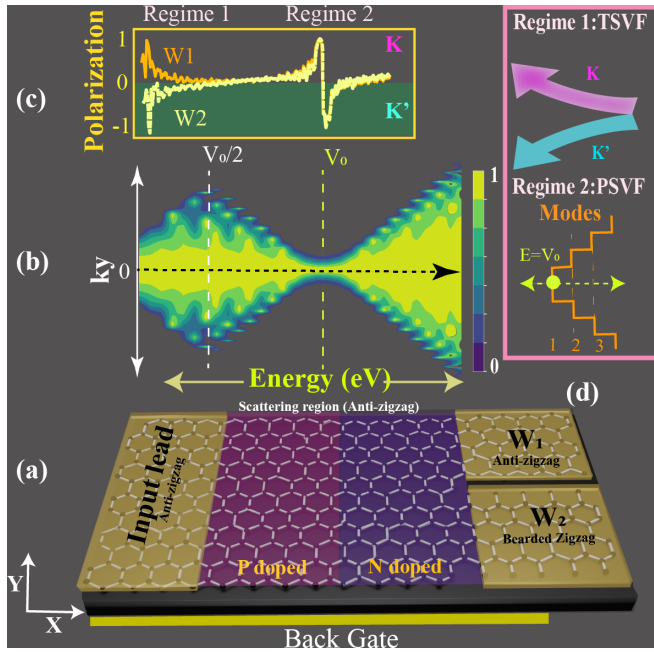
*bm@ee.iitb.ac.in

FIG. 1. Overview of our setup. (a) Schematic illustration of the proposed device comprising one input lead, two output leads, a device region with electrostatically doped p- and n-regions, and the back gate. The leads and the scattering region are antizigzag graphene, while the output lead W_2 is bearded graphene. (b) Transmission spectrum as a function of k_y. The maximum transmission value is unity and is depicted by bright yellow, while reflection is shown by deep blue. (c) The device shows two regimes of polarization: Regimes 1 and 2. (d) Regime 1, identified as a terminal-specific valley filter (TSVF), is due to band-structure engineering; Regime 2, identified as a parity-specific valley filter (PSVF), is due to the odd parity of zigzag atomic rows along the width governed by the parity selection rules.

hand, is based on the parity of the number of zigzag atomic rows giving rise to the valley-filter effect. The geometrical parameters of the device influencing the polarization in this regime reveal intriguing physics that contribute to it.

The paper is organized as follows. Section II describes the modeling and simulation of the device in detail. Section III is devoted to the results and a discussion, with Sec. III A discussing in detail the polarization in Regime 1, and Sec. III B discussing the polarization in Regime 2. Section III B also provides insights into the optimization of the maximum polarization conditions. The effects of varying the input width with respect to the width of the scattering region and the variation of the lengths of the p and n regions are analyzed. Section IV discusses in detail the performance evaluation of the device polarization in the presence of short-range Anderson disorder for different strengths of edge and bulk disorders. Finally, the main conclusions and outlook are laid out in Sec. V.

II. DEVICE AND SIMULATIONS DETAILS

The schematic diagram of the proposed device is shown in Fig. 1(a). It consists of one input lead, two output leads (W_1 and W_2), and a scattering region. The scattering region, the input lead, and the output lead W_1 consist of antizigzag

graphene, while the output lead W_2 consists of bearded graphene. A zigzag GNR having an odd number of atomic rows "N" is termed antizigzag graphene. When the Klein nodes are attached on both the edges of zigzag graphene, it is termed bearded graphene, which is shown in Fig. 1(a), W_2. The width and length of the scattering region are 70 and 100 nm, respectively, with $N \sim 329$ (it can be any odd number corresponding to width). The width of the input lead is generally equal to the width of the scattering region. The width of the two output leads is about half the width of the scattering region. The scattering region is electrostatically doped to form a symmetric abrupt PNJ. The Fermi level lies 0.25 eV below the Dirac point for the p region and above for the n region. The back gate is used to tune the energy range for device operation.

The simulations are carried out using the scattering matrix formalism [51]. The scattering matrix approach is then implemented within the Landauer-Büttiker formalism, where the entire structure is partitioned into several sections along the length, such that the transport across the consecutive sections is ballistic. For each section, a scattering matrix is formed which relates the amplitudes of an incoming wave to the outgoing wave for each mode. The cascading of these matrices yields the overall scattering matrix for the entire structure. The transmission amplitudes for all propagating modes are directly obtained from this scattering matrix, which is then used to calculate the current in a linear and a nonlinear response regime, provided the transport is phase-coherent [52]. The Hamiltonian represented in the second quantization form is constructed using the tight-binding model for graphene given by

$$\hat{H} = -t \sum_{i,j} \hat{c}_i^\dagger \hat{c}_j + \text{H.c.}, \tag{1}$$

where t is a hopping integral across the nearest neighbor i, j with the energy equal to -2.7 eV. Here, H.c. stands for the Hermitian conjugate, $\hat{c}_i^{(\dagger)}$ annihilates (creates) an electron at a site i on sublattice A (B), and the value of the lattice constant a is set to be 0.246 nm.

The valley-resolved transmission is calculated for both output leads W_1 and W_2, which are annotated as T_{K_1} and $T_{K_1'}$ for K and K' in W_1 and T_{K_2} and $T_{K_2'}$ in W_2, respectively [49]. The polarization $P_{1,2}$ in the leads W_1 and W_2 is given by

$$P_{1,2} = \frac{T_{K_{1,2}} - T_{K_{1,2}'}}{T_{K_{1,2}} + T_{K_{1,2}'}}. \tag{2}$$

The total transmission T through the device is given by the sum of both K and K' components from both outputs leads W_1 and W_2, given by

$$T = T_{K_1} + T_{K_2} + T_{K_1'} + T_{K_2'}. \tag{3}$$

Using this formulation, we compute the transmission across the output leads of the device for various parameters. Figure 1(b) shows the transmission spectra for one input/output lead PNJ configuration. The device is translation-invariant along the y direction, thus conserving the k_y component of the wave vector while transmitting across PNJ. A carrier with normal incidence tunnels through the barrier irrespective of its height and width due to the pseudospin conservation. This peculiar transport results in zero

backscattering for normal incidence, known as Klein tunneling [53–55]. From the transmission plot, it can be inferred that the spectra of k_y values increase with increasing energy in the low-energy regime. When the incident electron's energy is equal to half the barrier height, $(V_0/2)$, the conditions for the evanescent wave and critical angle are met. Thereby, with a further increase in energy, higher k_y components in transmission are suppressed. At the energy equal to barrier energy (V_0), also known as grazing energy, only normal components, i.e., $k_y = 0$, transmit with unity probability, otherwise transmission is through evanescent waves. Around the grazing energy, the device shows polarization in Regime 2.

Figure 1(c) shows the polarization with a clear demarcation between two polarization regimes. The polarization in Regime 1 is due to the band-structure engineering (TSVF), while that in Regime 2 is due to the odd parity of the zigzag ribbon governed by the parity selection rules (PSVF), as summarized in Fig. 1(d). The polarization at two output leads in Regime 1 is opposite, i.e., one corresponds to K and the other to K' due to output lead configuration. In Regime 2, both output leads correspond to the same polarization, which may be either K or K' depending on whether the energy level is just above or below the Fermi level. The interesting transport physics in each of the polarization regimes will be discussed henceforth.

III. RESULTS AND DISCUSSION

A. Regime 1: Terminal-specific valley filter

The valley-selective transmission at the output leads over a given energy range is attributed to the band-structure engineering. To understand transport physics, it is crucial to discuss the lattice structure and the corresponding band-structure properties of the graphene nanoribbons used. As mentioned earlier, two types of lattice configurations are used in the proposed device: (i) an antizigzag and (ii) bearded zigzag graphene.

Figures 2(a) and 2(b) show the lattice structures and computed $E - k$ relations for each of the configurations. The zigzag lattice with an odd number of zigzag atomic rows (N) is known as antizigzag graphene. The difference between a zigzag (N is even) and an antizigzag (N is odd) GNR lies in the transport properties of the edge states across the pn interface. The lattice structure is called a bearded zigzag lattice when the Klein nodes are attached to the zigzag-edged graphene. Both lattice structures have different sublattice atoms at the two edges, and the finite overlap of these edge wave functions gives rise to the specialized edge states. In Figs. 2(a) and 2(b), the edge states are highlighted by dark blue lines, while the bulk states are depicted by magenta and light blue lines, respectively.

These specialized edge states manifest as a partially flat region over a finite k range, giving rise to a substantial density of states (DOS) at the Fermi level. The range of k over which a flat band exists varies for each lattice type, as observed in the $E - k$ dispersion plots. For the antizigzag edge GNR, edge states are completely flat over the $2\pi/3 < |k| < \pi$ range and are dispersive for k values in the first Brillouin zone. The range of k over which edge states are completely flat for the bearded zigzag GNR is $0 < |k| < 2\pi/3$. The energy range over which
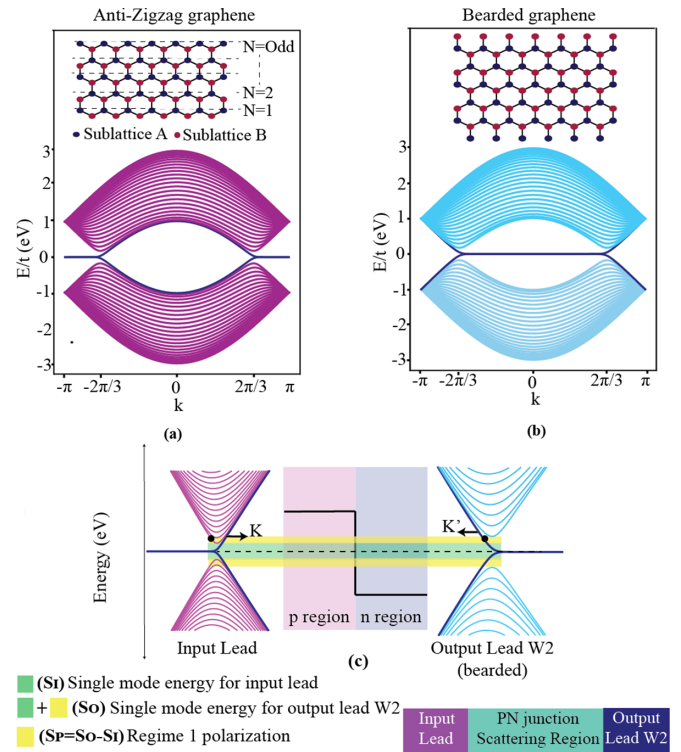

FIG. 2. The TSVF regime: Band structures of (a) zigzag and (b) bearded graphene with corresponding lattice configurations shown in the insets. The range of k over which the flat band exists is depicted by dark blue lines and is different for each of the lattice types. (c) Schematic of the transport through the device for output lead W_2, made up of bearded graphene and half the width of the input lead. The green-shaded region shows the single-mode energy range for the input lead. The single-mode energy range for the W_2 lead comprises the yellow and green shaded areas. This range is larger than that for the input lead due to its smaller width.

only edge states conduct is between the bulk states, i.e., the second lowest of the conduction band and the second highest energy state of the valance band. Over this energy range, the edge states provide a single mode for conductance. The energy range is called a single-mode energy (SME) range. The SME range is dependent on the physical dimension of the device, like the width, and is given by [56]

$$\Delta_S = 4t \cos \left(\frac{N-1}{2N+1} \pi \right). \quad (4)$$

We schematically present the transport mechanism when antizigzag (input) and bearded (output) graphene leads are adjoined at either side of a pn-junction in Fig. 2(c). It shows the band structure at the input side (on the left), the scattering region (in the middle), and the band structure of an output lead (on the right). The SME range for an input lead S_I, shown by the green shaded energy range, is smaller as compared to the SME of output lead S_O shown by the yellow+green shaded area. The energy range shown by the green color in regions 1 and 3 corresponds to single-mode operation, whereas region 2 has multiple modes because of doping.

The terminal-specific valley transmission depends on the polarity of the edge-state slope in the $E - k$ dispersion of
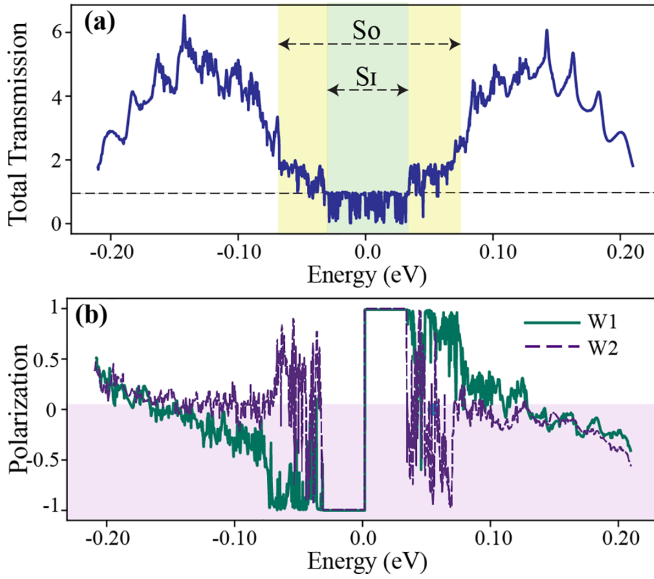
FIG. 3. Transmission and valley polarization in the TSVF regime. (a) Total transmission plot and (b) polarization plot as a function of electron energy. The single-mode energy range for input lead S_I (green) and output lead S_O (yellow + green) are highlighted. In the S_I range, the polarization is the same for both output leads. For the S_O energy range, the polarization is different in each output lead.

an output lead. For the output leads W_1 (antizigzag) and W_2 (bearded-zigzag), the polarity of an edge-state slope at the Dirac points (i.e., at $|k| = 2\pi/3$) is opposite, as shown in Figs. 2(a) and 2(b) by dark blue lines. In the energy range marked by yellow in Fig. 2(c), the input lead operates in the multimode regime with both positive and negative moving states, while the output leads are still in the SME range. A multimode operation is also observed across the PNJ due to significant doping. Therefore, a single allowed transmitting state at each output is either positive (K) or negative (K') based on the positive or negative edge state slope. Due to the opposite polarity of the edge state slope, two output leads can transmit two valleys in the yellow energy range.

Figure 3 shows the total transmission of the proposed structure and valley polarization. The total transmission as a function of the energy of the incoming electron is plotted in Fig. 3(a). In the SME regime (shown in green), the total transmission through the device is unity combining both of the output leads. In the multimode energy (MME) regime (yellow), the total transmission through the device is 2 as both of the output leads have a single mode available contributing unity each to the total transmission. It is worth noting that the transmission value is dominated by the region with the lowest number of modes.

The dip in the total transmission plot is due to backscattering, which is prominent near zero energy. The backscattering occurs due to a mismatched boundary across the heterointerface between zigzag and bearded graphene. The backscattering decreases the conductance and degrades the polarization value at the output lead W_2 [56]. Figure 3(b) shows the polarization plot that manifests the valley-selective functionality at the output leads.
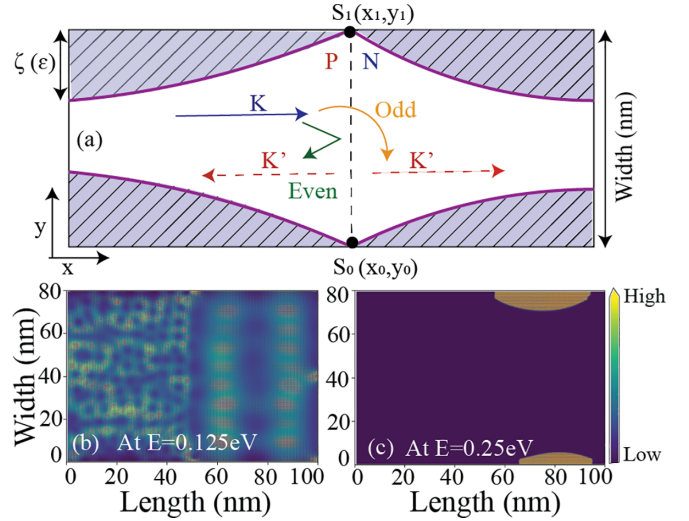

FIG. 4. The PSVF regime: parity-selective transmission condition and LDOS plots. (a) The shaded region shows the transverse extent ζ of the edge states in the device as a function of the device width W and the electron kinetic energy, ε. At zero kinetic energy, states are localized at the edges, and the black dots show the span of wave-vector interval. For zigzag graphene, with N being even, the incoming K state is reflected as a K' state, giving rise to the valley valve effect. For an odd value of N, the incoming state is transmitted as a K' state, leading to the valley filter effect for the lowest energy mode. (b) LDOS plot at $E = 0.125$ eV and at (c) $E = 0.25$ eV shows different distributions; LDOS is accumulated at the device edges for $E = 0.25$ eV.

B. Regime 2: Parity-specific valley filter in a multimode setup

Intervalley scattering is typical to graphene PNJs with zigzag edges, regardless of whether the interface region is sharp or atomically smooth [57]. The reason for intervalley scattering is localized edge states, which are the lowest energy modes. The edge states connect two different valleys, so the incoming and outgoing states come from different valleys. The wave vector across the PNJ can get transmitted (valley filter effect) or reflected (valley valve effect) without the flipping of valleys. Thus, the scattering over the PNJ must change the valleys in order to maintain the current flow. In our simulations, we consider a sharp PNJ profile. The edge states are completely localized at the zigzag edges of the device. The transverse extent ζ of the edge states along the width of the device depends on the kinetic energy of the incoming electron ε, which is given by

$$\varepsilon = E_F - V_0, \tag{5}$$

$$\zeta(\varepsilon) = W / \ln|\varepsilon W / v_f \hbar|. \tag{6}$$

The shaded region with hashed lines in Fig. 4(a) shows the transverse extent ζ of the edge-state wave vector k as a function of kinetic energy ε and the device width W as given in Eq. (6). Here, E_f is the Fermi energy, V_0 is the barrier height, $\hbar$ is Planck's constant, and v_f is the Fermi velocity. The width ζ decreases as the kinetic energy decreases and attains its minimum at zero kinetic energy. This minimum is of the order equivalent to the lattice constant a as shown by the points S_0 and S_1 in Fig. 4(a). The wave vector of the edge state spans the

interval of order $1/a$ between K and K', thereby facilitating intervalley scattering processes. An incoming state, say K (blue) at the interface (dashed line), switches to K' state while being transmitted or reflected, assisted by the intervalley scattering. The transmission or reflection of an incoming state depends on the parity of N. For even N, the parity of sublattice states across the PNJ is not the same, thus the intervalley scattering reflects an incoming state. This configuration manifests the valley valve effect for the lowest energy state. In the case of odd N, the sublattice states across PNJ are of the same parity, giving rise to the valley filter effect by transmitting an incoming state. The complete derivation and discussion regarding the parity selection rule are elaborated in [57–59].

The LDOS plots at two different carrier energies are shown in Figs. 4(b) and 4(c). The LDOS is uniformly distributed in the device at $E = 0.125$ eV, as can be seen in Fig. 4(b), whereas, at the grazing energy of $E = 0.25$ eV, only the edge states conduct up to the single channel energy range, which is localized at the edges of the device. Thus, the charge density is accumulated at the device edges, as depicted in Fig. 4(c). It can be inferred that the main contribution to the conductance is through the edges for a single-channel energy range. Thus, interesting polarization effects or even complete valley-switching of the electronic states can be realized by tailoring the edge states at the input and output leads of a graphene PNJ.

We now focus our discussion on how the width of the input lead and the lengths of p- and n-doped regions influence the transmission and valley polarization in the regime of multimode operation. The multimode state is referred for the input side. Although at grazing energy the device operates with a single mode, the degree of polarization has a strong dependence on the way input modes approach the PNJ. So, it is essential to consider the behavior of carriers in graphene for analyzing the way input modes approach the interface.

Low-energy carriers in graphene behave as relativistic particles, and therefore a PNJ exhibits an electronic analog of Snell's law and Veselago lensing. Following the optics analogy, the input lead in the multimode setup acts as an optical slit, and its width determines the angular dispersion of the incoming modes at the PN interface. We consider two cases: Case A: When the width of the input lead is equal to the width of the device, as illustrated in Fig. 5. Case B: When the input lead width is half and centered along the device width, as seen in Fig. 6. The ray trace in Fig. 5 shows that all the electron trajectories are parallel to the device edges and are perpendicular to the PNJ interface throughout the width of the device. The ray trace in Fig. 6 shows the ray dispersion along the lead edges. The rays are perpendicular in the middle of the device width and diverge out towards the edges along the PN interface (see Appendix A).

The degree of valley filtering also depends on the doping profile in the PNJ. First, the doping level decides the energy range where polarization is observed. Second, the length of the doped regions is equivalent to the potential barrier width in respective energy ranges. A narrow barrier width allows conventional tunneling through it. Thus, here we have considered the effect of barrier width variation along with the input lead variation for optimizing the conditions to achieve maximum polarization.
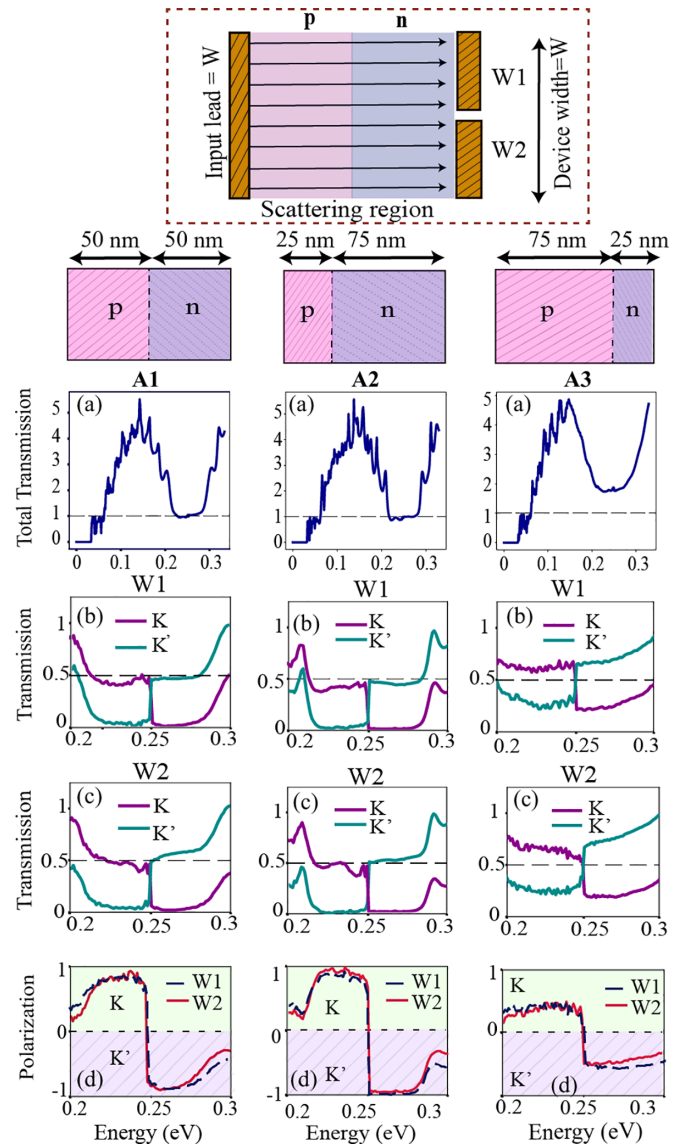

FIG. 5. Case A: Width of the input lead equal to the width of the scattering region. The ray trace shows that the carrier trajectories coming from the input lead are parallel throughout the width of the device. With respect to the input lead, three junction positions, at A1: 50 nm, A2: 25 nm, and A3: 75 nm, have been considered. For each of these device configurations, (a) the total transmission plot, transmission for K and K' at output leads (b) W_1 and (c) W_2, and (d) polarization are shown. For the positive energy range, the length of the n-region affects the transmission and polarization value. The length of the n-region is sufficiently large for devices A1 and A2. Over the single-mode energy range, the total transmission value is 1 and attains the maximum polarization. In device A3, the length of the n-region is small, and due to the quantum tunneling, the total transmission value is above 1, and the overall polarization value degrades.

For the variation in the length of the doped region, the transmission in the device simplifies to the transport calculations through the potential barrier in graphene. In the positive energy range, the length of the n-region acts as the barrier width, and for the negative energy range, the p-region length acts as the barrier width. In a graphene PNJ, the transmission
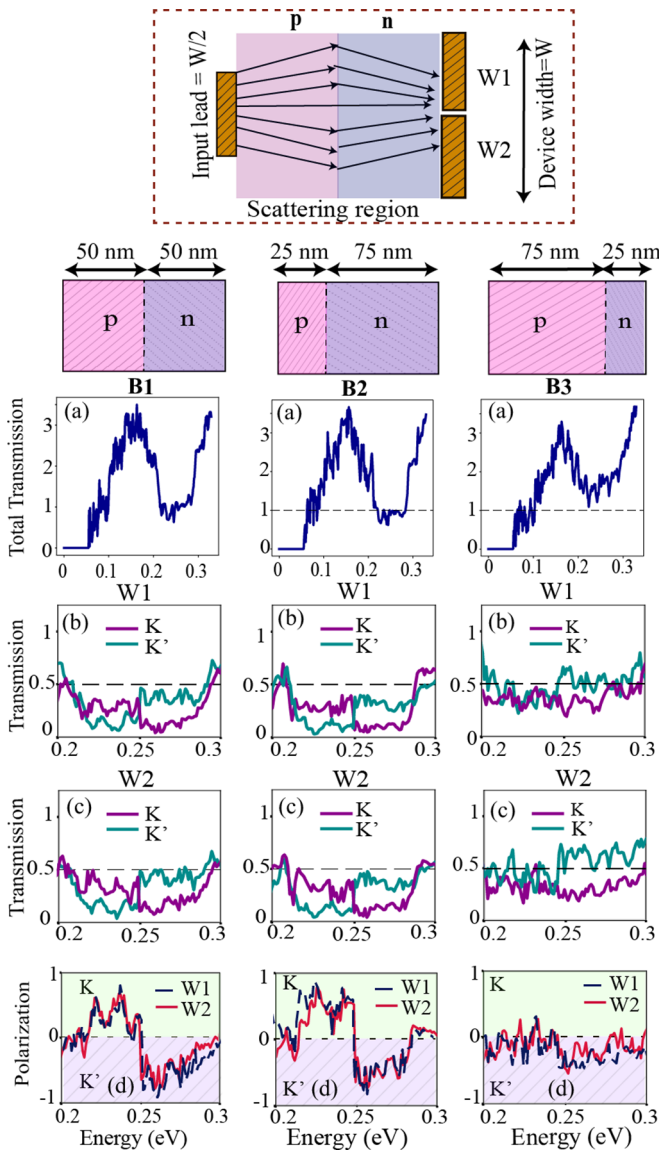
FIG. 6. Case B: The width of the input lead is half the width of the scattering region. The ray trace shows that the carrier trajectories coming from the input lead spread out across the width of the device. Similar to the earlier case, three device configurations, with junction positions at B1: 50 nm, B2: 25 nm, and B3: 75 nm, have been considered. For each of these device configurations, (a) the total transmission plot, transmission for K and K' at output leads (b) W_1 and (c) W_2, and (d) polarization are shown. The total transmission value is lower than in the previous case due to the lower number of modes present at the input lead. For devices B1 and B2 (wider n-region), the total transmission value is approximately 1 in the single mode energy range, while for device B3 (narrower n-region) it is above 1 due to the quantum tunneling. There is a finite transmission for K and K' in each case, and so the polarization degrades. The worst-case polarization is observed for device B3 due to the combined effect of dispersed carrier trajectories and quantum tunneling.

probability of an incoming wave depends on the angle of incidence with respect to the PN interface. Above the critical angle, the incident wave is totally reflected. The critical angle condition is realized when the energy of an incoming electron E is greater than half the barrier height. When the critical

angle condition is met, the evanescent waves are formed, and total internal reflection results in total reflection for the PNJ. On the contrary, in the case of the potential barrier, evanescent waves appear in the barrier region and give rise to quantum tunneling [53]. So, the narrower the barrier region, the higher the quantum tunneling, which comprises the tunneling of both the K and K' components. This has direct implications on the degree of polarization at the output lead.

We now elaborate on the results shown in Figs. 5 and 6. The position of the PNJ is varied along the device length. We have considered three device configurations represented as A(B)1, A(B)2, and A(B)3, wherein the junction is positioned at 50, 25, and 75 nm, respectively, from the input lead. The total transmission plots, i.e., the sum of K and K' transmission components from both output leads, are shown by A(B)i(a), where $i = 1, 2, 3$. The A(B)i(b and c) show the transmission of K and K' components in output lead W_1 and W_2, respectively. And finally, the A(B)i(d) shows the polarization at both output leads.

The total transmission plots for all three cases show an increase in transmission value with an increase in electron energy as a number of modes get added. When the electron energy reaches half the potential height, i.e., 0.125 eV, the critical angle condition is formed and the higher angular modes are suppressed. When the energy of the incoming carrier approaches the potential barrier height, i.e., 0.25 eV, only edge states conduct and pseudospin conservation is valid only for the normal incident case. Thus, in SME the total transmission value for A1(a) and A2(a) is unity, while for case A3(a) it is higher than 1 and the transmission curve is smooth, which shows that the transmission is via quantum tunneling due to a narrower n-region. With a pseudo-spin-conserved transmission, the total transmission in the SME range is 1. For two output leads, the maximum transmission value is half for K and K' as observed in A1(b and c) and A2(b and c). But for A3(b and c) the value is slightly higher for both K and K' components, which in turn degrades the polarization. The polarization is maximum in A2(d) and slightly lower in A1(d). The polarization dropped to nearly half its maximum value for case A3(d) due to the quantum tunneling.

For case B, i.e., when the width of an input lead is half that of the scattering region, the results are similar to that in the previous case. But, now as the input lead width is half of what it was in the previous case, the maximum total transmission is smaller. This is because of the lower number of modes present in the input lead. As of the previous case, the transmission in cases B1(a) and B2(a) in the single-mode energy range is approximately equal to unity, while in B3(a) it is higher because of quantum tunneling due to the narrower n region. The transmission of K and K' in W_1 and W_2, plotted in B1(b and c) and B2(b and c), shows the flickering curve due to quantum tunneling because of a reduced wave-function amplitude at the edges coupled with an angle-selective transmission at the PN interface (Appendix A). The incidence angle at the PN interface is related to the input lead width and the diffraction effect. A large dispersion angle from the input lead edge results in reduced wave-function amplitude at the PN interface. At grazing energy, only normally incident wave functions can conserve pseudospin across the PN interface, otherwise the transmission is dominated by quantum

tunneling. In quantum tunneling, there is a finite transmission probability of both valleys, and thus the polarization in B1(d) and B2(d) is lower as compared to the A1(d) and A2(d) cases. The worst polarization B3(d) is due to the combined effects of the narrower n-region and dispersed electron trajectories because of the variation of the input lead.

Thus, the conditions for achieving the maximum polarization could be summarized as follows: (i) Zigzag-edged graphene should have odd parity for N to allow intervalley scattering across the PNJ interface and achieve polarization at the lowest energy mode, i.e., edge states. (ii) The edge states conducting during a single-mode energy range are completely localized at the physical device edges [60,61]. (iii) At grazing energy, only normally incident electrons have complete transmission probability, otherwise the transmission is via evanescent waves or through quantum tunneling. So, to get maximum polarization, the electron should be incident normally at the PN interface and especially at the edges of the device where LDOS is concentrated. If the electron is incident at an angle other than the normal angle, first because of the diffraction effect the amplitude is reduced, and secondly, due to angle-selective transmission across the PN interface at grazing energy, the quantum tunneling probability increases and polarization degrades.

IV. ROLE OF SHORT-RANGE ANDERSON DISORDER

In graphene, quantum transport properties are significantly affected by perturbations due to underlying symmetries and uneven edges [62]. In terms of the experimental realization of the proposed device structure, we note that fabrication-induced disorders like edge roughness, dislocations, impurity atoms, scatterers, and defects may lead to unavoidable nonidealities. We now analyze the sensitivity of the valley polarization due to such nonidealities by augmenting the effect of disorders in an ideal device structure.

We introduce a short-range Anderson disorder along the device edges and the scattering region. The Anderson short-range disorder is defined as distribution-based potential fluctuations introduced to the on-site energies of the π-orbitals [63]. It is called a short-range disorder because the lengthscale over which the disorder potential varies is smaller than a lattice constant. The presence of short-range potential fluctuations forms local PNJs. In zigzag edge graphene, locally formed PNJs lead to intervalley scattering and zero backscattering, thus locally breaking the time-reversal symmetry (TRS) while preserving it as a whole [64–66].

We have introduced the Anderson short-range disorder in two ways, one along the edges and the other in the bulk. The uncorrelated disorder potential is uniformly distributed, and the final on-site potential is given by

$$\epsilon_{(e,b)} = \epsilon_i + \delta\epsilon_{(e,b)}, \tag{7}$$

where the subscript e, b corresponds to the edge disorder and the bulk disorder, respectively. The quantity $\delta\epsilon_{e,b} = [-\gamma/2, \gamma/2]$, where γ is the strength of the disorder potential and ϵ_i is the on-site energy due to electrostatic doping. For edge disorder, we have considered three atomic row thicknesses on both edge sides, and we introduced the scattering potential over p- and n-electrostatically doped regions. For the
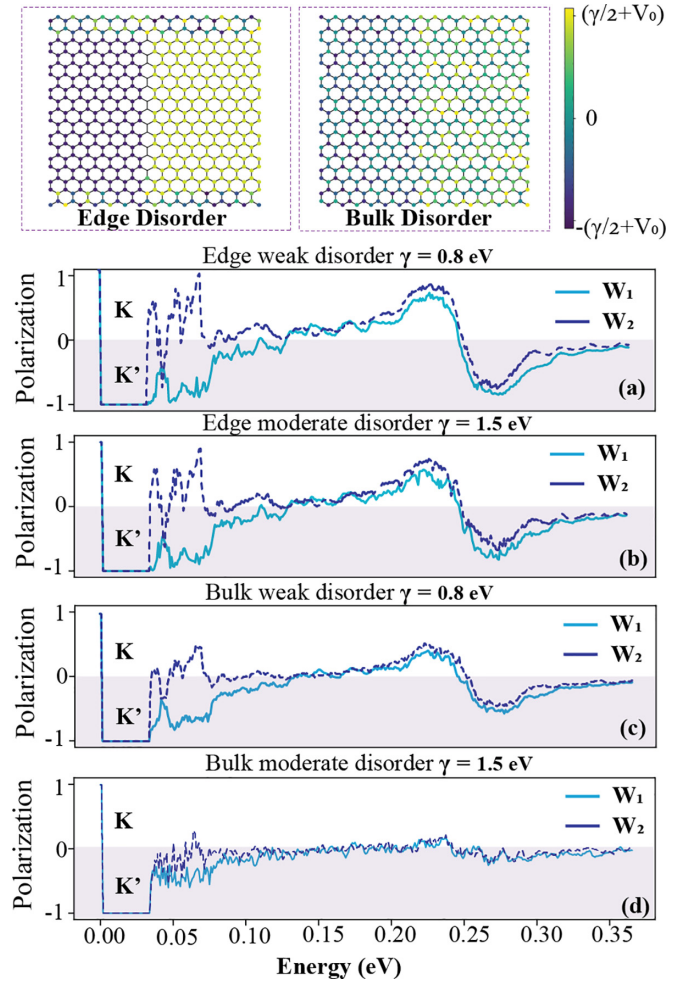

FIG. 7. Valley polarization plots with the introduction of edge and bulk Anderson short-range disorder of both weak and moderate disorder strengths for (a) weak edge disorder with strength $\gamma = 0.8$ eV, (b) moderate edge disorder with strength $\gamma = 1.5$ eV, (c) weak bulk disorder with strength $\gamma = 0.8$ eV, and (d) moderate bulk disorder with strength $\gamma = 1.5$ eV. The bulk disorder has a significant effect on the polarization for increasing disorder strength

bulk disorder, similarly, we have introduced the $\delta\epsilon_b$ potential all over the scattering region [67].

For a given hopping integral value $t = -2.7$ eV, the disorder strength in the range of [0.26–1] eV is considered to be a weak disorder, whereas the values ranging around [1.35,2.7] are taken as strong. Here, we have considered the two values of the disorder strength $\gamma = 0.8$ and 1.5 eV, which are classified as weak and moderate disorders, respectively. To average the effects of the different spatial distributions of the disorder potential, we simulate and average the results of 40 configurations of each type.

Figures 7(a) and 7(b) show the polarization plots for edge disorder with weak and moderate strengths. It can be inferred that the polarization slightly degrades with increasing disorder strength but mostly withstands the edge-disorder effect. This can be attributed to the presence of a large LDOS accumulated near the charge neutrality point in a narrow energy range confined at the edges. Thus, when the carriers are injected with energy states above the narrow energy spectrum, but

within the SME range, they avoid edges, leaving these strips immune to edge disorder [68]. Figures 7(c) and 7(d) represent bulk disorder with weak and moderate disorder strength. For bulk disorder, even for a weaker strength, the transmission (not shown) is significantly affected and thereby results in the polarization plot noted in Fig. 7(c). At moderate strengths, the polarization completely vanishes as shown in Fig. 7(d). Thus, the polarization is more immune to edge disorder in comparison with bulk disorder at different disorder strengths. Here, we have considered the case of the input lead width being equal to that of the scattering region. The results would show much inferior performance for the case when the input lead is half that of the scattering region.

V. CONCLUSION

In this work, we proposed an all-electrical valley polarizer using zigzag edge graphene nanoribbons in a multiterminal device geometry that can be gate-tuned to operate along two independent regimes: (i) a terminal-specific valley filter that utilizes band-structure engineering, and (ii) a parity-specific valley filter that exploits the parity selection rule in zigzag edge graphene. We showed that the device exhibits intriguing physics in the multimode regime of operation that affects the valley polarization, and hence we investigate various factors affecting the polarization in wide device geometries, such as an optical analog of graphene Dirac fermions, angle-selective transmission via p-n junctions, and the localization of edge states. We optimized the geometry of the proposed device to achieve maximum valley polarization, thereby paving the way toward a physics-based tunable valleytronic device design with monolayer graphene. The performance of the proposed device was evaluated in the presence of Anderson short-range disorder at the edges and the bulk. The polarization was quite resistant to edge disorder compared to bulk disorder at various disorder strengths. The proposed concepts can also be extended to the photonic crystals [69] for the experimental implementation of a valley polarizer without the requisite polarized light.

APPENDIX A: DIFFRACTION

Dirac fermions in graphene obey the laws of ray optics, such as Snell's law, and exhibit Veselago lensing. It is important to note that the incoming electron trajectory must have a finite angle with respect to the axis perpendicular to the PN interface for exhibiting the Veselago lensing and negative refraction effect [70,71]. However, for the normal incidence, fermions just transmit through the barrier following Klein tunneling. The angular dispersive behavior of graphene fermions is the result of diffraction [72,73].
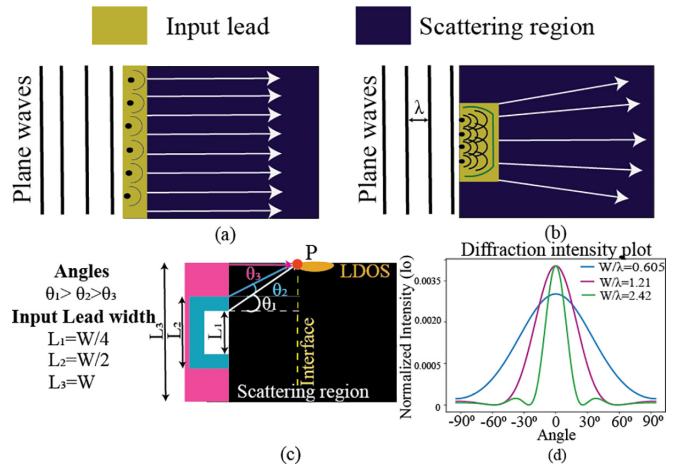

FIG. 8. Optical slit analogy. (a) No diffraction is observed when the input lead and the scattering region have the same width. (b) Ray diffracts when the input lead width is smaller than the scattering region. (c) For increasing lead widths, the angle between the axis normal to the interface from the lead top end point and the point P at the interface end points at device edges decreases. (d) Intensity distribution plot for different input lead widths at a constant wavelength.

In our work, we show that the input lead acts as an optical slit for incoming modes in the scattering region. When the width of the input lead is equal to the scattering region width, there is no diffraction and all modes are parallel to each other [Fig. 8(a)]. In the case of the smaller width of the input lead, the electron trajectories show a diffraction effect. There is bending at the edges of the input lead for an incoming mode resulting in angular dispersion of the electron trajectory [Fig. 8(b)].

For an incident intensity of I_0, the intensity distribution in the diffracted orders is given by [74]

$$I = I_0 \left[\frac{\sin(\beta/2)}{\beta/2} \right]^2, \tag{A1}$$

where W is the width of the slit, the wavelength of the Dirac fermion with energy E is $\lambda = h v_f / E$, where $v_f = 10^6$ m/s, and the angle θ is the angle from the point of interest, i.e., P (in red) [Fig. 8(c)] to the axis perpendicular to the slit plane shown by the white dashed line. The β is the total phase difference between the two rays approaching from the top and bottom of the slit to point P. The path difference between the ray from the top of the slit to the ray in the middle of the slit with width W is $W/2 \sin \theta$. Thus, $W \sin \theta$ is equal to twice the difference between the top and bottom rays. The phase difference is $2\pi/\lambda$ times the path difference. Thus, the total phase difference can be written as $\beta = 2\pi/\lambda * (W \sin \theta)$. The expression of intensity in terms of angle θ is

$$I = I_0 \left[\frac{\sin[\pi W (\sin \theta)/\lambda]}{\pi W (\sin \theta)/\lambda} \right]^2. \tag{A2}$$

The plot Fig. 8(d) shows the intensity distribution as a function of angle θ and the W/λ ratio. Here, we considered the value of $E = 0.25$ eV, $\lambda = 16.52$ nm, and we varied the value of width W. The ratios $W/\lambda = 0.6, 1.21, 2.42$ are plotted in pink, blue, and green, respectively, in Fig. 8(d). From the plot,

it can be observed that the curve for $W/\lambda = 0.6$ is widespread over the angular spectrum. As the width W increases, the intensity gets maximized in zeroth order suppressing higher-order side lobes.

Consider an example with different widths of input lead L1, L2, and L3 with respect to scattering region width W as shown in Fig. 8(c). In Fig. 8(c), the smallest slit gives the largest diffraction angle (θ_1) with some amount of intensity being distributed in the corresponding diffracted orders [blue curve in Fig. 8(d)]. Thus, the electron wave function reaches point P with a finite angle and reduced amplitude. Again by angular selective transmission at the PN interface, there is a further reduction in the transmission. At grazing energy, the conductance is mostly due to quantum tunneling.

Similarly, if we consider the case with equal widths of both regions, there is no diffraction. At grazing energy, Klein tunneling contributes to single-mode conductance due to an antizigzag configuration with a lesser probability of quantum tunneling. Figures 8(a) and 8(b) show the ray trace for equal and smaller input lead width, respectively, which forms the basis for the explanation of the results.

APPENDIX B: TRANSMISSION ACROSS THE PN INTERFACE UNDER DIFFERENT SCENARIOS

1. Doped region length variation: Transmission across a potential barrier

The PNJ has highly angle-dependent transmission. The transmission coefficient vanishes after a certain angle, called a critical angle. The condition for a critical angle is

$$\sin\theta = \frac{V_0 - E}{E}. \tag{B1}$$

Beyond the critical angle, evanescent waves are present on another side of the junction, and total reflection is observed. In the case of the potential barrier, once the condition of the critical angle is reached, the evanescent wave penetrates the other side of the junction. Unlike the PNJ, there is no total reflection in the case of barrier potential. The presence of a second junction in the barrier case allows the wave to be transmitted through the barrier via quantum tunneling with diminished amplitude.

2. Quantum tunneling at grazing energy

The transmission of the carrier arriving with energy E, which is exactly equal to barrier energy, is via evanescent waves except for normal incidence. The transmission probability decreases with an increase in incident angle. Thus, for the maximum polarization, there must be a normal incidence in which pseudospin is conserved, while in quantum tunneling the transmission probability is the same for both K and K'. Thus, the polarization is lowered. A detailed explanation for transmission across PNJ and a barrier is provided in Ref. [53]. Note: The polarization results for Regime 2 are valid with input and one output lead device setup also, while the polarization in Regime 1 requires a different output lead configuration for showing opposite valley polarization.

[1] S. A. Vitale, D. Nezich, J. O. Varghese, P. Kim, N. Gedik, P. Jarillo-Herrero, D. Xiao, and M. Rothschild, Valleytronics: opportunities, challenges, and paths forward, Small **14**, 1801483 (2018).

[2] Y. S. Ang, S. A. Yang, C. Zhang, Z. Ma, and L. K. Ang, Valleytronics in merging dirac cones: All-electric-controlled valley filter, valve, and universal reversible logic gate, Phys. Rev. B **96**, 245410 (2017).

[3] M. Schirber, Valley-polarized jets in graphene, Physics **14**, s80 (2021).

[4] J.-B. Qiao, Z.-D. Chu, L.-M. Wu, and L. He, Quantum superposition states of two valleys in graphene, arXiv:1408.5230.

[5] J. R. Schaibley, H. Yu, G. Clark, P. Rivera, J. S. Ross, K. L. Seyler, W. Yao, and X. Xu, Valleytronics in 2D materials, Nat. Rev. Mat. **1**, 16055 (2016).

[6] J. Xia, X. Wang, B. K. Tay, S. Chen, Z. Liu, J. Yan, and Z. Shen, Valley polarization in stacked MoS_2 induced by circularly polarized light, Nano Res. **10**, 1618 (2017).

[7] A. Friedlan and M. M. Dignam, Valley polarization in biased bilayer graphene using circularly polarized light, Phys. Rev. B **103**, 075414 (2021).

[8] F. Caruso, M. Schebek, Y. Pan, C. Vona, and C. Draxl, Chirality of valley excitons in monolayer transition-metal dichalcogenides, J. Phys. Chem. Lett. **13**, 5894 (2022).

[9] K. M. McCreary, M. Currie, A. T. Hanbicki, H.-J. Chuang, and B. T. Jonker, Understanding variations in circularly polarized photoluminescence in monolayer transition metal dichalcogenides, ACS Nano **11**, 7988 (2017).

[10] M. S. Mrudul, Á. Jiménez-Galán, M. Ivanov, and G. Dixit, Light-induced valleytronics in pristine graphene, Optica **8**, 422 (2021).

[11] O. V. Gamayun, V. P. Ostroukh, N. V. Gnezdilov, İ. Adagideli, and C. W. J. Beenakker, Valley-momentum locking in a graphene superlattice with y-shaped kekulé bond texture, New J. Phys. **20**, 023016 (2018).

[12] F. Zhan, B. Zheng, X. Xiao, J. Fan, X. Wu, and R. Wang, Magnetic field induced valley-polarized quantum anomalous Hall effects in ferromagnetic van der Waals heterostructures, Phys. Rev. B **105**, 035131 (2022).

[13] H. Pan, Z. Li, C.-C. Liu, G. Zhu, Z. Qiao, and Y. Yao, Valley-Polarized Quantum Anomalous Hall Effect in Silicene, Phys. Rev. Lett. **112**, 106802 (2014).

[14] C. Zhao, T. Norden, P. Zhang, P. Zhao, Y. Cheng, F. Sun, J. P. Parry, P. Taheri, J. Wang, Y. Yang *et al.*, Enhanced valley splitting in monolayer WSe_2 due to magnetic exchange field, Nat. Nanotech. **12**, 757 (2017).

[15] J. Zhou, Q. Sun, and P. Jena, Valley-Polarized Quantum Anomalous Hall Effect in Ferrimagnetic Honeycomb Lattices, Phys. Rev. Lett. **119**, 046403 (2017).

[16] S. Refaely-Abramson, D. Y. Qiu, S. G. Louie, and J. B. Neaton, Defect-Induced Modification of Low-Lying Excitons and Valley Selectivity in Monolayer Transition Metal Dichalcogenides, Phys. Rev. Lett. **121**, 167402 (2018).

[17] Y. Liu, J. Song, Y. Li, Y. Liu, and Q.-F. Sun, Controllable valley polarization using graphene multiple topological line defects, Phys. Rev. B **87**, 195445 (2013).

[18] D. Gunlycke and C. T. White, Graphene Valley Filter Using a Line Defect, Phys. Rev. Lett. **106**, 136806 (2011).

[19] S. Wang, M. S. Ukhtary, and R. Saito, Strain effect on circularly polarized electroluminescence in transition metal dichalcogenides, Phys. Rev. Res. **2**, 033340 (2020).

[20] M. Chauwin, Z. B. Siu, and M. B. A. Jalil, Strain-Modulated Graphene Heterostructure as a Valleytronic Current Switch, Phys. Rev. Appl. **17**, 024035 (2022).

[21] Z. Wu, F. Zhai, F. M. Peeters, H. Q. Xu, and K. Chang, Valley-Dependent Brewster Angles and Goos-Hänchen Effect in Strained Graphene, Phys. Rev. Lett. **106**, 176802 (2011).

[22] S. P. Milovanović and F. M. Peeters, Strain controlled valley filtering in multi-terminal graphene structures, Appl. Phys. Lett. **109**, 203108 (2016).

[23] X. W. Zhao, Y. Li, R. D. Liang, G. C. Hu, X. B. Yuan, and J. F. Ren, Enhanced valley polarization at valence/conduction band in transition-metal-doped WTe$_2$ under strain force, Appl. Surf. Sci. **504**, 144367 (2020).

[24] S. Zhao, X. Li, B. Dong, H. Wang, H. Wang, Y. Zhang, Z. Han, and H. Zhang, Valley manipulation in monolayer transition metal dichalcogenides and their hybrid systems: status and challenges, Rep. Prog. Phys. **84**, 026401 (2021).

[25] W.-T. Hsu, Y.-L. Chen, C.-H. Chen, P.-S. Liu, T.-H. Hou, L.-J. Li, and W.-H. Chang, Optically initialized robust valley-polarized holes in monolayer WSe$_2$, Nat. Commun. **6**, 8963 (2015).

[26] S. Feng, C. Cong, S. Konabe, J. Zhang, J. Shang, Y. Chen, C. Zou, B. Cao, L. Wu, N. Peimyoo *et al.*, Engineering valley polarization of monolayer WS$_2$: a physical doping approach, Small **15**, 1805503 (2019).

[27] Y. Ye, J. Xiao, H. Wang, Z. Ye, H. Zhu, M. Zhao, Y. Wang, J. Zhao, X. Yin, and X. Zhang, Electrical generation and control of the valley carriers in a monolayer transition metal dichalcogenide, Nat. Nanotech. **11**, 598 (2016).

[28] B. T. Zhou, K. Taguchi, Y. Kawaguchi, Y. Tanaka, and K. T. Law, Spin-orbit coupling induced valley Hall effects in transition-metal dichalcogenides, Commun. Phys. **2**, 26 (2019).

[29] Z. Yu, Z.-Y. Ong, S. Li, J.-B. Xu, G. Zhang, Y.-W. Zhang, Yi Shi, and X. Wang, Analyzing the carrier mobility in transition-metal dichalcogenide MoS$_2$ field-effect transistors, Adv. Funct. Mater. **27**, 1604093 (2017).

[30] K. I. Bolotin, K. J. Sikes, Z. Jiang, M. Klima, G. Fudenberg, J. Hone, P. Kim, and H. L. Stormer, Ultrahigh electron mobility in suspended graphene, Solid State Commun. **146**, 351 (2008).

[31] S. Y. Zhou, G.-H. Gweon, A. V. Fedorov, P. N. de First, W. A. De Heer, D.-H. Lee, F. Guinea, A. H. Castro Neto, and A. Lanzara, Substrate-induced bandgap opening in epitaxial graphene, Nat. Mater. **6**, 770 (2007).

[32] T. Zhou, S. Cheng, M. Schleenvoigt, P. Schüffelgen, H. Jiang, Z. Yang, and I. Žutić, Quantum Spin-Valley Hall Kink States: From Concept to Materials Design, Phys. Rev. Lett. **127**, 116402 (2021).

[33] D. Xiao, W. Yao, and Q. Niu, Valley-Contrasting Physics in Graphene: Magnetic Moment and Topological Transport, Phys. Rev. Lett. **99**, 236809 (2007).

[34] Z. Qiao, S. A. Yang, B. Wang, Y. Yao, and Q. Niu, Spin-polarized and valley helical edge modes in graphene nanoribbons, Phys. Rev. B **84**, 035431 (2011).

[35] C. Yesilyurt, S. G. Tan, G. Liang, and M. B. A. Jalil, Perfect valley filter in strained graphene with single barrier region, AIP Adv. **6**, 056303 (2016).

[36] F. Zhai, X. Zhao, K. Chang, and H. Xu, Magnetic barrier on strained graphene: A possible valley filter, Phys. Rev. B **82**, 115442 (2010).

[37] F. Zhai, Valley filtering in gapped graphene modulated by an antisymmetric magnetic field and an electric barrier, Nanoscale **4**, 6527 (2012).

[38] W.-T. Lu, Valley-dependent band structure and valley polarization in periodically modulated graphene, Phys. Rev. B **94**, 085403 (2016).

[39] L. S. Cavalcante, A. Chaves, D. R. Da Costa, G. A. Farias, and F. M. Peeters, All-strain based valley filter in graphene nanoribbons using snake states, Phys. Rev. B **94**, 075432 (2016).

[40] D. Zhai and N. Sandler, Local versus extended deformed graphene geometries for valley filtering, Phys. Rev. B **98**, 165437 (2018).

[41] S.-Y. Li, Y. Su, Y.-N. Ren, and L. He, Valley Polarization and Inversion in Strained Graphene via Pseudo-Landau Levels, Valley Splitting of Real Landau Levels, and Confined States, Phys. Rev. Lett. **124**, 106802 (2020).

[42] Y. Wu, D. Zhai, C. Pan, B. Cheng, T. Taniguchi, K. Watanabe, N. Sandler, and M. Bockrath, Quantum wires and waveguides formed in graphene by strain, Nano Lett. **18**, 64 (2018).

[43] C.-C. Hsu, M. L. Teague, J.-Q. Wang, and N.-C. Yeh, Nanoscale strain engineering of giant pseudo-magnetic fields, valley polarization, and topological channels in graphene, Sci. Adv. **6**, eaat9488 (2020).

[44] T. Low and F. Guinea, Strain-induced pseudomagnetic field for novel graphene electronics, Nano Lett. **10**, 3551 (2010).

[45] J. J. Wang, S. Liu, J. Wang, and J.-F. Liu, Valley filter and valve effect by strong electrostatic potentials in graphene, Sci. Rep. **7**, 10236 (2017).

[46] M. M. Asmar and S. E. Ulloa, Minimal geometry for valley filtering in graphene, Phys. Rev. B **96**, 201407(R) (2017).

[47] J. M. Pereira, F. M. Peeters, R. N. Costa Filho, and G. A. Farias, Valley polarization due to trigonal warping on tunneling electrons in graphene, J. Phys.: Condens. Matter **21**, 045301 (2009).

[48] J. L. Garcia-Pomar, A. Cortijo, and M. Nieto-Vesperinas, Fully Valley-Polarized Electron Beams in Graphene, Phys. Rev. Lett. **100**, 236801 (2008).

[49] K. Jana and B. Muralidharan, Robust all-electrical topological valley filtering using monolayer 2D-xenes, npj 2D Mater. Appl. **6**, 19 (2022).

[50] S. Banerjee, K. Jana, A. Basak, M. S. Fuhrer, D. Culcer, and B. Muralidharan, Robust Subthermionic Topological Transistor Action via Antiferromagnetic Exchange, Phys. Rev. Appl. **18**, 054088 (2022).

[51] C. W. Groth, M. Wimmer, A. R. Akhmerov, and X. Waintal, Kwant: a software package for quantum transport, New J. Phys. **16**, 063065 (2014).

[52] S. Bandyopadhyay and M. Cahay, The generalized scattering matrix approach: An efficient technique for modeling quantum transport in relatively large and heavily doped structures, in

Computational Electronics, The Springer International Series in Engineering and Computer Science, Vol. 113, edited by K. Hess, J. P. Leburton, and U. Ravaioli (Springer, Boston, MA, 1991).

[53] P. E. Allain and J.-N. Fuchs, Klein tunneling in graphene: optics with massless electrons, Eur. Phys. J. B **83**, 301 (2011).

[54] C. W. J. Beenakker, Colloquium: Andreev reflection and klein tunneling in graphene, Rev. Mod. Phys. **80**, 1337 (2008).

[55] M. I. Katsnelson, K. S. Novoselov, and A. K. Geim, Chiral tunneling and the klein paradox in graphene, Nat. Phys. **2**, 620 (2006).

[56] K. Wakabayashi, Electronic transport properties of nanographite ribbon junctions, Phys. Rev. B **64**, 125428 (2001).

[57] A. R. Akhmerov, J. H. Bardarson, A. Rycerz, and C. W. J. Beenakker, Theory of the valley-valve effect in graphene nanoribbons, Phys. Rev. B **77**, 205416 (2008).

[58] A. Cresti, G. Grosso, and G. P. Parravicini, Valley-valve effect and even-odd chain parity in *p-n* graphene junctions, Phys. Rev. B **77**, 233402 (2008).

[59] A. Rycerz, J. Tworzydło, and C. W. J. Beenakker, Valley filter and valley valve in graphene, Nat. Phys. **3**, 172 (2007).

[60] K. Nakada, M. Fujita, G. Dresselhaus, and M. S. Dresselhaus, Edge state in graphene ribbons: Nanometer size effect and edge shape dependence, Phys. Rev. B **54**, 17954 (1996).

[61] M. Fujita, K. Wakabayashi, K. Nakada, and K. Kusakabe, Peculiar localized state at zigzag graphite edge, J. Phys. Soc. Jpn. **65**, 1920 (1996).

[62] E. R. Mucciolo and C. H. Lewenkopf, Disorder and electronic transport in graphene, J. Phys.: Condens. Matter **22**, 273201 (2010).

[63] S.-J. Xiong and Y. Xiong, Anderson localization of electron states in graphene in different types of disorder, Phys. Rev. B **76**, 214204 (2007).

[64] A. Lherbier, B. Biel, Y.-M. Niquet, and S. Roche, Transport Length Scales in Disordered Graphene-Based Materials: Strong Localization Regimes and Dimensionality Effects, Phys. Rev. Lett. **100**, 036803 (2008).

[65] K. Wakabayashi, Y. Takane, and M. Sigrist, Perfectly Conducting Channel and Universality Crossover in Disordered Graphene Nanoribbons, Phys. Rev. Lett. **99**, 036601 (2007).

[66] J. Wurm, M. Wimmer, and K. Richter, Symmetries and the conductance of graphene nanoribbons with long-range disorder, Phys. Rev. B **85**, 245418 (2012).

[67] G. Schubert, J. Schleede, and H. Fehske, Anderson disorder in graphene nanoribbons: A local distribution approach, Phys. Rev. B **79**, 235116 (2009).

[68] D. A. Areshkin, D. Gunlycke, and C. T. White, Ballistic transport in graphene nanostrips in the presence of disorder: Importance of edge effects, Nano Lett. **7**, 204 (2007).

[69] Z. Gao, Z. Yang, F. Gao, H. Xue, Y. Yang, J. Dong, and B. Zhang, Valley surface-wave photonic crystal and its bulk/edge transport, Phys. Rev. B **96**, 201402(R) (2017).

[70] K. J. A. Reijnders and M. I. Katsnelson, Diffraction catastrophes and semiclassical quantum mechanics for veselago lensing in graphene, Phys. Rev. B **96**, 045305 (2017).

[71] V. V. Cheianov, V. Fal'ko, and B. L. Altshuler, The focusing of electron flow and a veselago lens in graphene pn junctions, Science **315**, 1252 (2007).

[72] P. Darancet, V. Olevano, and D. Mayou, Coherent Electronic Transport through Graphene Constrictions: Subwavelength Regime and Optical Analogy, Phys. Rev. Lett. **102**, 136803 (2009).

[73] G.-H. Lee, G.-H. Park, and H.-J. Lee, Observation of negative refraction of dirac fermions in graphene, Nat. Phys. **11**, 925 (2015).

[74] H. D. Young and R. A. Freedman, *University Physics with Modern Physics* (Pearson Education, 2015).